

Intrinsically Ultrastrong Light-Matter Interactions in Crystalline Films of Carbon Nanotubes

Po-Hsun Ho, Damon B. Farmer, George S. Tulevski, Shu-Jen Han, Douglas M. Bishop, Lynne M. Gignac, Jim Bucchignano, Phaedon Avouris, Abram L. Falk*
IBM T. J. Watson Research Center, Yorktown Heights, NY

Abstract:

When optical emitters are strongly coupled to optical cavities, light and matter mix and lose their distinct characteristics¹. To date, strong light-matter coupling has only been observed in hybrid systems, where cavities and emitters are separate objects. Here, we show that carbon nanotubes can be crystallized into chip-scale superlattices and that this new material enables intrinsically ultrastrong light-matter interactions: rather than interacting with external cavities, nanotube excitons couple to the near-infrared Fabry–Pérot plasmon resonances^{2–5} of the nanotubes themselves. Our crystallized nanotube films have a hexagonal crystal structure, ~25 nm domains, and a 1.74 nm lattice constant. This extremely high nanotube density allows plasmon-exciton coupling strengths to reach 0.5 eV, which is 75% of the bare exciton energy and a record for light-matter interactions at room temperature. Crystallized nanotube films provide a compelling foundation for high-ampacity conductors⁶, low-power optical switches⁷, tunable metamaterials⁸, and thresholdless nanolasers⁹.

Main Text:

The physical world is normally divided into light and matter. However, in cavity quantum electrodynamics, strongly coupled emitters hybridize with a cavity's photon field through vacuum Rabi oscillations¹⁰, and these hybridized excitations have both matter-like and light-like attributes.

If the Rabi-oscillation frequency (Ω) is so fast that it approaches the resonance frequencies of the emitters (ω_0) and the cavity, the system has reached ultrastrong coupling¹¹. Instead of the cavity and emitters exchanging energy one quanta at a time, a single cavity photon can then borrow energy from the vacuum field and excite two or more emitters. Technologically,

* E-mail: alfalk@us.ibm.com

ultrastrong coupling could lead to single-photon nonlinearities that provide a pathway from fundamental concepts in quantum electrodynamics to advanced telecommunications hardware⁷.

Systems that have achieved strong or ultrastrong light-matter coupling include dielectric and metallic resonators coupled to atoms⁹, quantum dots¹², fluorescent molecules^{13–15}, carbon nanotubes^{16–18}, and superconducting qubits¹⁹. However, all demonstrations of strongly coupled systems have been hybrid systems, where emitters and optical cavities are near each other but separate objects. In these hybrid systems, coupling strengths are limited by both the emitters' density and their spatial overlap with the cavity.

In this work, we crystallize films of carbon nanotubes into superlattices to generate a material that exhibits intrinsically ultrastrong light-matter interactions. Instead of coupling to external cavities, nanotube excitons (the “matter”) couple to internal nanotube plasmon resonances (the “light”). These plasmon resonances, comprising longitudinal Fabry–Pérot charge oscillations along the nanotubes, are notable for their electrostatic tunability and ability to confine light to a small mode volume^{3,4,20}. As a result of these small volumes, the extremely high density of nanotubes, and the nearly ideal plasmon-exciton spatial overlap deriving from the intrinsic nature of the light-matter interactions, the normalized plasmon-exciton interaction strengths reach $\Omega/\omega_0 = 75\%$. They are thus far into the ultrastrong regime, which is typically defined by $\Omega/\omega_0 \gtrsim 30\%$,¹¹ and unprecedented at room temperature.

Nanotube superlattices could play an exciting role in active, nonlinear optical devices. They could lead to tunable nanolasers in which the gain medium is intrinsically built into the lasing cavity. Moreover, $\chi^{(3)}$ optical nonlinearities, already strong in dispersed carbon nanotubes, should be dramatically enhanced by ultrastrong light-matter coupling⁸. From a fundamental electromagnetics standpoint, the highly anisotropic optical properties of nanotube superlattices could make them a resource for hyperbolic metamaterials with a negative index of refraction²¹. Outside of photonics, they could have diverse applications like high-ampacity conductors⁶ and battery anodes²². Their successful assembly is a milestone in the larger endeavor of assembling nanostructures into macroscopic functional materials.

Our crystallized nanotube films are fabricated using controlled vacuum filtration²³. A powder of arc-discharge single-wall carbon nanotubes, whose average diameter is 1.41 nm, is dispersed in water with the surfactant sodium dodecylbenzenesulfonate (see Methods). Atomic force microscopy confirms that the nanotubes are unbundled in solution (Supplementary Fig. S1).

A very weak vacuum then slowly pulls the suspension through a polycarbonate membrane, causing the nanotubes to self-organize and align in the plane of the membrane. The membrane is then dried (Supplementary Fig. S2) and the 1 inch-in-diameter nanotube films are transferred to silicon or sapphire substrates.

Surprisingly, the nanotubes in these solution-assembled films can crystallize into superlattices. Cross-sectional transmission electron microscopy (TEM) of a 200-nm-thick film shows a two-dimensional hexagonal superlattice of nanotubes, with at least 50% of the nanotubes crystallized (Figs. 1a-c and Supplementary Fig. S3). Despite evident polycrystallinity, domain sizes are large, approximately 25 nm. Selected area TEM diffraction confirms the hexagonal lattice structure (Fig. 1d).

Grazing-incidence X-ray diffraction (XRD) spectroscopy provides further verification of the film's crystallinity (Figs. 1d and Supplementary Fig. S4). The prominent XRD peak at $2\theta = 5.8^\circ$, which is 15 times stronger than that from a control film of randomly oriented nanotubes, corresponds to an inter-nanotube lattice constant of 1.74 nm and a two-dimensional nanotube density of $3.8 \times 10^5 \mu\text{m}^{-2}$. For context, crystallization of nanotubes has also been seen in naturally but randomly produced nanotube ropes generated during nanotube growth²⁴. However, large-area crystalline films have not previously been observed, nor have nanotube superlattices been observed to self-assemble in solution.

To investigate their plasmon-exciton interactions²⁵, we etch the nanotube superlattices into nanoribbon Fabry-Pérot plasmon resonators (Figs. 1e and 2a) and study them with μ -Fourier-transform infrared (μ -FTIR) spectroscopy. Approximately 10^8 nanotubes are in each μ -FTIR measurement area. The lowest energy semiconducting-nanotube exciton, the S_{11} exciton, has a center energy of $\hbar\omega_0 = 0.66$ eV and an inhomogeneous linewidth of $\hbar\Gamma_0 = 0.2$ eV (Fig. 2b).

Exposing the nanotubes to HNO_3 vapor, a strong oxidizer, induces a high density of positive charge carriers²⁶ that deplete the nanotube valence band and quench the transition strength of S_{11} . Vacuum annealing can then reverse this process by eliminating the adsorbates. The on-axis resistivity of our crystallized films then increases by a factor of 30 (from $\rho = 2.6 \times 10^{-4}$ ohm-cm to $\rho_0 = 7.8 \times 10^{-3}$ ohm-cm, see Supplementary Information), and S_{11} is re-strengthened.

In their highly doped state, the nanotube resonators have a strong single extinction peak corresponding to plasmon resonance (Fig. 2c)^{4,5}. As expected from the nanoribbon geometry, the

resonance frequency (ω_p) is approximately proportional to \sqrt{tq} ^{5,27}, where t is the out-of-plane nanoribbon thickness, and q is the wavenumber, defined as π/L , where L is the etched length of the nanotubes. Since the S_{11} exciton is suppressed in this highly doped state, ω_p crosses unperturbed through ω_0 as L is reduced.

In their annealed, resistive state, the nanotube resonators have peaks corresponding to both ω_0 and ω_p , with $\hbar\Gamma_p$ ranging from 0.1 – 0.2 eV. In this state, as L is reduced, a large anticrossing between ω_p and ω_0 becomes evident (Fig. 2d). This anticrossing is the key signature of strong coupling. Near the anticrossing, the bare ω_p and ω_0 resonances hybridize to form ω_{\pm} polaritons (Fig. 2e). The Rabi splitting, $\hbar\Omega$, which we compute as the experimentally measured minimum of $\hbar(\omega_+ - \omega_-)$, reaches 0.485 eV for $t = 49$ -nm resonators. In slightly thinner resonators ($t = 37$ nm, see Fig. 3), $\hbar\Omega = 0.50$ eV, and $\Omega/\omega_0 = 75\%$.

The normalized coupling strength between the plasmon-exciton polaritons (“plexcitons”) is thus significantly beyond the ultrastrong-coupling threshold. In fact, it exceeds that of any room-temperature system known to date, the previous record being the $\Omega/\omega_0 = 62\%$ observed when organic dye molecules are coupled to silver microcavities¹⁵. For carbon nanotubes coupled to external cavities, $\Omega/\omega_0 = 12\%$ has been attained and $\Omega/\omega_0 \sim 70\%$ predicted to be achievable¹⁸. At cryogenic temperatures, the record light-matter coupling strength is $\Omega/\omega_0 = 130\%$, achieved using superconducting qubits coupled to superconducting resonators¹⁹.

A distinctive feature of carbon-nanotube plasmons is their exceptional tunability. Length, thickness, and doping level are all tuning factors, allowing ω_p to span frequencies from the terahertz up to the near infrared. Because doping level determines the exciton-transition strength, it modifies not only ω_p but also Ω (Fig. 3a,b). In turn, the tuning of Ω allows access to a broad range of polariton energies. This access could translate into electrically tunable optoelectronic devices like photodetectors, lasers, and quasi-coherent incandescent light sources.

Due to coupled antenna effects, thicker nanotube resonators have higher energies than thinner ones do⁵. The plasmon-exciton anticrossing can therefore be reached at smaller wavenumbers (i.e. higher L values) (Fig. 3c). Since the plasmonic mode volumes of thicker films are larger than those of thinner ones, their Rabi splittings are also modestly lower, though still extremely strong: a 260 nm-thick film exhibits $\Omega/\omega_0 = 60\%$. Their large dipole strength makes these thick films particularly suitable for optoelectronics.

The plasmon-exciton coupling can be described by a two-coupled-oscillator Hamiltonian:

$$H = \omega_p(a^\dagger a) + \omega_0(b^\dagger b) + \Omega(a^\dagger + a)(b^\dagger + b) + \Omega^2/\omega_0(a^\dagger + a)^2 \quad (\text{Eq. 1})$$

where a^\dagger (a) and b^\dagger (b) are the exciton and plasmon creation (annihilation) operators, respectively^{28,29}. The first two terms represent plasmon and exciton self-energies, and the second two terms represent plasmon-exciton interactions. Equation 1 includes counter-rotating interaction terms, which are neglected in the frequently used Jaynes-Cummings Hamiltonian, an approximation to Eq. 1, but must be considered in ultrastrong coupling. The full Hopfield solution^{28,29} to Eq. 1 is:

$$\omega^4 - \omega^2 \left((\omega_p - i\Gamma_p)^2 + (\omega_0 - i\Gamma_0)^2 + g^2 \right) + (\omega_p - i\Gamma_p)^2 (\omega_0 - i\Gamma_0)^2 = 0 \quad (\text{Eq. 2})$$

where g is the light-matter interaction parameter. To fit our data, we use Eq. 2, fix ω_0 , Γ_0 , and Γ_p to experimentally observed values, and parametrize ω_p as X_0/\sqrt{L} and g as X_1/\sqrt{L} , where X_0 and X_1 are fitting factors (see Methods). This model exhibits excellent agreement with all of our experimental data (see Figs. 2e, 3a, and 3c).

Highly conductive nanotube films can also exhibit strong light-matter interactions. At high energies, the $\omega_p \propto 1/\sqrt{L}$ relationship breaks down, and $\hbar\omega_p$ saturates at 0.9 eV (Fig. 3d). Though S_{11} is nearly completely suppressed at high doping levels, many higher energy nanotube excitons are not (see Supplementary Fig. S6). Consequently, even at high nanotube doping levels, the plasmons strongly interact with these higher energy excitons and have flat, saturating dispersion relationships. In the future, smaller diameter nanotubes could allow the 0.9 eV threshold to be crossed. However, our currently achieved tuning range already allows carbon-nanotube plasmonics to be applied to C-band near-infrared telecommunications.

Intrinsically ultrastrong coupling represents a compelling new concept in active nanophotonics. It could drive the next generation of tunable infrared devices, including nanoscale light sources, multispectral detectors, and wavefront-shaping chips based on tunable metamaterials. As ultrastrongly coupled systems, nanotube antennas could serve as physical representations of the Dicke Hamiltonian and a testbed for its quantum-phase transition to superradiance³⁰. In turn, superradiating antennas could function as bright single-photon sources

for quantum communications. Crystals of nanotubes could thus serve as a bridge between fundamental concepts in quantum optics and practical technologies.

Methods:

Fabrication of crystallized carbon-nanotube films

A vacuum filtration method is used to prepare the crystalline carbon nanotube films from suspensions of carbon nanotubes. This method is a modified version of the method used in Refs. 5 and 23. The setup consists of a fritted glass filter and a 15 mL funnel (Millipore XX1002500) purchased from Fisher Scientific Company. The vacuum filtration method consists of four steps:

1. Dispersing nanotubes in a surfactant solution
2. Modifying the surface of a filter membrane
3. Vacuum-filtering the nanotube suspension through the modified membrane
4. Transferring the nanotube film onto a target substrate

An arc-discharge powder of single wall carbon nanotubes, with average diameter of 1.41 nm, ~70% semiconducting purity, and an average length of 500 nm (P2-SWCNT, Carbon Solutions, Inc.), is dispersed into an aqueous solution of 0.4% (wt/vol) sodium dodecylbenesulfonate (SDBS, Sigma-Aldrich). The initial nanotube concentration is 0.4 mg/ml. Bath sonication is applied to the suspension for 15 minutes, followed by tip sonication for 45 minutes. During tip sonication, the suspension is immersed in cold water to prevent heating. The suspension is then centrifuged for 1 hour at 38,000 r.p.m to remove any remaining nanotube bundles and amorphous carbon. The supernatant is then diluted by a factor of 5 with deionized water, making the SDBS concentration approximately 0.08%. The suspension is then further diluted by a factor of 3 with 0.08% SDBS solution.

The filtration membranes for the vacuum filtration process (Whatman Nuclepore track-etched polycarbonate hydrophilic membranes, 0.05 μm pore size) are first treated with a 2 Torr air plasma for 30 seconds. This treatment provides a negative charge surface on the membrane, which proved to be an important step for achieving a high degree of nanotube alignment and high packing density. Oxygen plasma was also used, but whereas oxygen plasma would etch the membrane, air plasma is gentler and found to yield better results.

The nanotube suspension is then filtered through the plasma-treated membranes. For the first 3 mL solution, a weak vacuum pressure (2.8 Torr) is used to pull the suspension through the membrane at a very slow rate, approximately 0.4 mL/hour. This slow filtration speed gives the nanotubes enough time to align and to cover the whole membrane uniformly. After 3 mL has been pulled through the membrane, the vacuum pressure is increased to 8.4 Torr, which results in a filtration rate of 0.8 mL/hour. Finally, before the meniscus contacts the membrane, a high vacuum pressure of 370 Torr is applied to dry the liquid. The film thickness is observed to be proportional to the volume of the precursor used (14 nm per 1 mL of suspension). Supplementary Fig. S2 shows a photo of a membrane with a nanotube film.

The substrates used in this work are high-resistivity silicon and sapphire wafers. For the silicon substrates, the native oxide was first removed by buffered hydrofluoric acid to reduce the coupling of nanotube plasmons to optical phonons in the oxide⁴. A drop of water is placed on the substrate, and the membrane is then placed on the substrate with the nanotube surface face down. The membrane is then covered by a glass slide, and gentle pressure is applied to make the nanotube film adhere. The membrane is then dried with gentle N₂ gas. The membrane is then dissolved in chloroform. Finally, the nanotube film on the substrate is annealed at 500 °C in a vacuum oven at 10⁻⁷ Torr for 2 hours, which removes surfactant and polymer residue.

Fabrication of nanoribbons and charge-transfer doping

Conventional electron-beam lithography is used to pattern the CNT films. A bilayer resist consisting of a poly(methyl methacrylate) (PMMA) layer and a hydrogen silsesquioxane (HSQ) layer is spin-coated on the nanotube film. After e-beam exposure, the HSQ is developed as a hard mask. The PMMA layer and nanotubes are then etched with oxygen reactive ion etching. The residual PMMA and HSQ are then stripped with chloroform. The strip length to spacing ratio is fixed at 1:1, as shown in Fig. 2a.

To induce strong *p*-type surface-charge-transfer doping, the sample is exposed to HNO₃ vapor for 10 minutes. For a moderate doping level, the sample is first strongly doped and then annealed on a hot plate at 120 °C. The doping conditions 1-3 in Fig. 3a are respectively realized with heating times of 2, 7, and 30 minutes.

Characterization of films

The crystalline properties of nanotube films are characterized with a Siemens D5000 XRD spectrometer. The conductivities are measured by Keithley 2400 equipped with an in-line 4-probe system. The extinction spectra are all measured in a Bruker Nicolet 8700 μ -FTIR system, except for measurements of the high frequency plasmon resonances in thick films ($\nu_p > 7000$ cm^{-1} , see Fig. 3d), which are measured with a PerkinElmer Lambda 950 UV-VIS-NIR spectrometer.

Fitting the data to the Hopfield model

To perform the fits to Eq. 2, we fix ω_0 , Γ_0 , and Γ_p to experimentally observed values: 0.66 eV/\hbar , 0.1 eV/\hbar , and 0.1 eV/\hbar , respectively. We then parameterize ω_p as X_0/\sqrt{L} and g as X_1/\sqrt{L} , where X_0 and X_1 are fitting parameters. The ω_p parameterization derives from the dispersion of a quasi-2D nanoribbon.

The parameterization for g follows from the following reasoning. For strongly coupled ensembles of emitters, $g \propto \sqrt{Nf/\epsilon V}$, where N is the number of emitters, f is their oscillator strength, ϵ is the dielectric constant, and V is the mode volume²⁸. In our system, N is the number of nanotubes in a resonator and independent of L . We also approximate f as a constant with respect to L . The dielectric constant (ϵ) is proportional to the square of the effective index of refraction, which is proportional to $1/\sqrt{L}$. Finally, from the quasi-2D geometry, $V \propto L^2$. Putting these proportionalities together, we arrive at $g \propto 1/\sqrt{L}$.

With X_0 and X_1 as fitting parameters and ω_0 , Γ_0 , and Γ_p as fixed, experimentally derived parameters, we then fit Eq. 2 to the experimental data. To perform these fits, we used Matlab, by Mathworks, Inc., and its nonlinear least squares fitting algorithm.

References:

1. Kimble, H. J. The quantum internet. *Nature* **453**, 1023–1030 (2008).
2. Zhang, Q. *et al.* Plasmonic nature of the terahertz conductivity peak in single-wall carbon nanotubes. *Nano Lett.* **13**, 5991–5996 (2013).
3. De Vega, S., Cox, J. D. & De Abajo, F. J. G. Plasmons in doped finite carbon nanotubes

- and their interactions with fast electrons and quantum emitters. *Phys. Rev. B* **94**, 1–6 (2016).
4. Falk, A. L. *et al.* Coherent Plasmon and Phonon-Plasmon Resonances in Carbon Nanotubes. *Physical Review Letters* **118**, 257401 (2017).
 5. Chiu, K. C. *et al.* Strong and Broadly Tunable Plasmon Resonances in Thick Films of Aligned Carbon Nanotubes. *Nano Lett.* **17**, 5641–5645 (2017).
 6. Wang, X. *et al.* High-capacity power cables of tightly-packed and aligned carbon nanotubes. *Adv. Funct. Mater.* **24**, 3241–3249 (2014).
 7. Sanchez-Burillo, E., Zueco, D., Garcia-Ripoll, J. J. & Martin-Moreno, L. Scattering in the ultrastrong regime: Nonlinear optics with one photon. *Phys. Rev. Lett.* **113**, 1–5 (2014).
 8. Nikolaenko, A. E. *et al.* Carbon nanotubes in a photonic metamaterial. *Phys. Rev. Lett.* **104**, 153902 (2010).
 9. McKeever, J., Boca, A., Boozer, A. D., Buck, J. R. & Kimble, H. J. Experimental realization of a one-atom laser in the regime of strong coupling. *Nature* **425**, 268–271 (2003).
 10. Khitrova, G., Gibbs, H. M., Kira, M., Koch, S. W. & Scherer, A. Vacuum Rabi splitting in semiconductors. *Nat. Phys.* **2**, 81–90 (2006).
 11. Ciuti, C., Bastard, G. & Carusotto, I. Quantum vacuum properties of the intersubband cavity polariton field. *Phys. Rev. B* **72**, 115303 (2005).
 12. Yoshle, T. *et al.* Vacuum Rabi splitting with a single quantum dot in a photonic crystal nanocavity. *Nature* **432**, 200–203 (2004).
 13. Lidzey, D. G. *et al.* Strong exciton-photon coupling in an organic semiconductor microcavity. *Nature* **395**, 53–55 (1998).
 14. Fofang, N. T. *et al.* Plexcitonic Nanoparticles: Plasmon- Exciton Coupling in Nanoshell-J-Aggregate Complexes. *Nano Lett* **8**, 3481–3487 (2008).
 15. Barachati, F. *et al.* Tunable third-harmonic generation from polaritons in the ultrastrong coupling regime. *ACS Photonics* **5**, 119–125 (2018).
 16. Zakharko, Y. *et al.* Broadband Tunable, Polarization-Selective and Directional Emission of (6,5) Carbon Nanotubes Coupled to Plasmonic Crystals. *Nano Lett.* **16**, 3278–3284 (2016).
 17. Graf, A., Tropf, L., Zakharko, Y., Zaumseil, J. & Gather, M. C. Near-infrared exciton-

- polaritons in strongly coupled single-walled carbon nanotube microcavities. *Nat. Commun.* **7**, 13078 (2016).
18. Zakharko, Y., Graf, A. & Zaumseil, J. Plasmonic Crystals for Strong Light-Matter Coupling in Carbon Nanotubes. *Nano Lett.* **16**, 6504–6510 (2016).
 19. Yoshihara, F. *et al.* Superconducting qubit-oscillator circuit beyond the ultrastrong-coupling regime. *Nat. Phys.* **13**, 44–47 (2017).
 20. Shi, Z. *et al.* Observation of a Luttinger-liquid plasmon in metallic single-walled carbon nanotubes. *Nat. Photonics* **9**, 515–519 (2015).
 21. Poddubny, A., Iorsh, I., Belov, P. & Kivshar, Y. Hyperbolic metamaterials. *Nat. Photonics* **7**, 958–967 (2013).
 22. Casas, C. De & Li, W. A review of application of carbon nanotubes for lithium ion battery anode material. *J. Power Sources* **208**, 74–85 (2012).
 23. He, X. *et al.* Wafer-scale monodomain films of spontaneously aligned single-walled carbon nanotubes. *Nat. Nanotechnol.* **11**, 633–638 (2016).
 24. Thess, A. *et al.* Crystalline Ropes of Metallic Carbon Nanotubes. *Science (80-.)*. **273**, 483–487 (1996).
 25. Bondarev, I. V, Woods, L. M. & Tatur, K. Strong exciton-plasmon coupling in semiconducting carbon nanotubes. *Phys. Rev. B* **80**, 85407 (2009).
 26. Zhou, W. *et al.* Charge transfer and Fermi level shift in p-doped single-walled carbon nanotubes. *Phys. Rev. B* **71**, 205423 (2005).
 27. Low, T. & Avouris, P. Graphene plasmonics for terahertz to mid-infrared applications. *ACS Nano* **8**, 1086–1101 (2014).
 28. Todisco, F. *et al.* Ultrastrong Plasmon-Exciton Coupling by Dynamic Molecular Aggregation. *ACS Photonics* **5**, 143–150 (2018).
 29. Hopfield, J. J. Theory of the contribution of excitons to the complex dielectric constant of crystals. *Phys. Rev.* **112**, 1555–1567 (1958).
 30. Wang, Y. K. & Hioe, F. T. Phase transition in the dicke model of superradiance. *Phys. Rev. A* **7**, 831–836 (1973).

Acknowledgments: The authors thank Kuan-Chang Chiu, Jerry Tersoff, James Hannon, Jessie Rosenberg, Xiaowei He, Weilu Gao, and Junichiro Kono for helpful discussions. This work was

funded by IBM and the Postdoctoral Research Abroad Program of the Ministry of Science and Technology Taiwan (NSC 106-2917-I-564-012).

Author contributions: P.H. fabricated the crystallized films and performed the optical measurements. G.T. helped to purify the nanotube suspensions. L.M.G. performed the TEM measurements. J.B. performed the electron-beam lithography. D.M.B. helped to perform the XRD measurements. All authors participated in analyzing the data and writing the paper.

Supplementary Information accompanies this paper.

Competing interests: The authors declare no competing interests.

Figures:

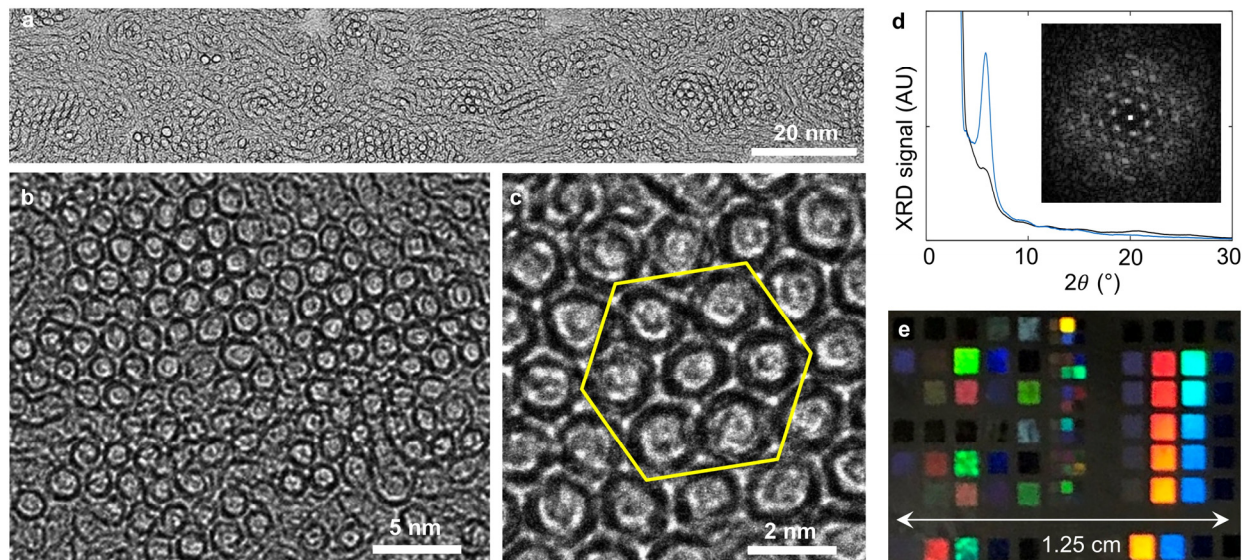


Figure 1 | Crystallized carbon-nanotube films. a-c. Cross-sectional TEM images of the crystallized nanotube films at three magnifications. **d.** Grazing-incidence XRD spectrum of a crystallized nanotube film (blue curve), and a control film of randomly oriented nanotubes (black curve). The peak at $2\theta = 5.8^\circ$ corresponds to an inter-nanotube lattice spacing of 1.74 nm. The x-ray beam size is 2 cm^2 . Inset: Selected-area TEM diffraction image of the region in Fig. 1c, confirming the hexagonal lattice structure. **e.** A photo of a crystallized film after it is etched into gratings of nanoribbons. The color of diffracted light varies based on the pitch ($2L$, see Fig. 2a) of the grating.

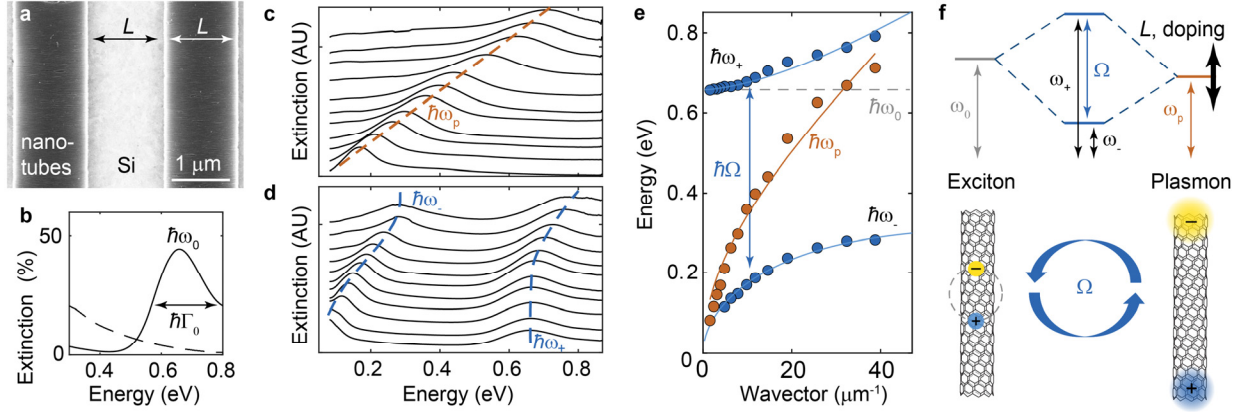


Figure 2 | Intrinsically ultrastrong light-matter interactions. **a.** A scanning electron micrograph of a crystallized nanotube film etched into Fabry–Pérot plasmon resonators. **b.** The extinction spectra of an annealed, resistive film (solid line), showing a strong S_{11} -exciton peak, and a highly chemically doped film (dashed line), where S_{11} is quenched. The film thickness is $t = 49$ nm. **c.** Extinction spectra of plasmon resonators etched into this film, with a fixed, high doping level and varying lithographically defined nanotube lengths (L values). For clarity, each curve is vertically offset and normalized by its maximum (see Supplementary Fig. S5 for un-normalized curves). From top to bottom, $L = (80, 100, 130, 175, 225, 260, 325, 400, 500, 650, 800)$ nm. The dashed line is a guide for the eye. **d.** In their annealed, resistive state, the nanotube resonators have extinction spectra with two peaks each, corresponding to the two polariton branches. **e.** Orange: Peak energy of the highly doped plasmon resonators from Fig. 2c vs. wavevector (q), defined as $q = \pi/L$. The solid line is a fit to $\omega_p \propto \sqrt{q}$. Blue: Peak energies of the plasmon-exciton polaritons from Fig. 2d, showing an anticrossing with a Rabi splitting of $\Omega = 0.485$ eV. The solid line is a fit to Eq. 2. **f.** Depiction of the nanotube excitons hybridizing with the nanotube plasmons to form ultrastrongly coupled plasmon-exciton polaritons.

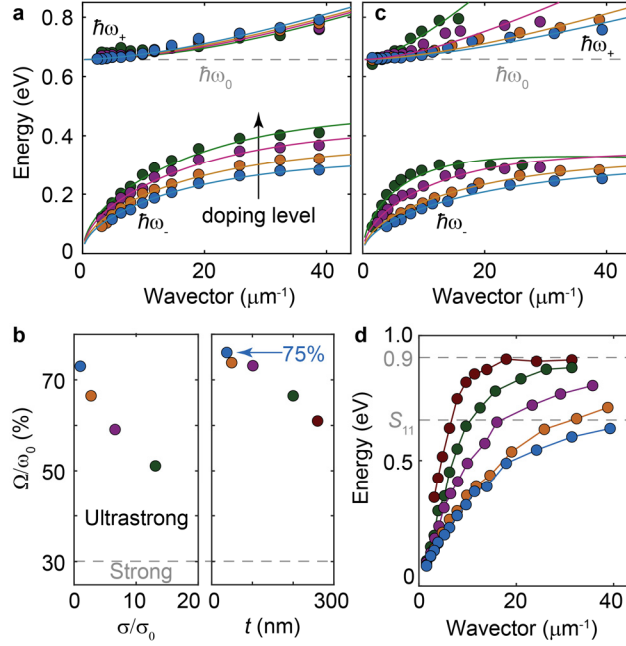


Figure 3 | Tunability of light-matter interactions. **a.** Polariton energies vs. wavevector for resonators at 4 different doping levels / conductivity levels: $\sigma = (1, 2.7, 6.6, \text{ and } 13.1) \times \sigma_0$, with $\sigma_0 = 1/\rho_0$, and σ color coded to match 3b(left). The film thickness is $t = 49$ nm. **b.** Left: Ω vs. film conductivity (σ), with t fixed to 49 nm. Right: Ω vs t , with σ fixed to σ_0 (i.e. the minimum doping level that we could access) **c.** Polariton energies of resonators as a function of q and t , with t color coded to match Fig. 3b(right) and σ fixed to σ_0 . **d.** Resonator energies when the resonators are highly doped. The five curves correspond to the five film thicknesses plotted in Fig. 3b(right): $t = (37, 49, 101, 200, \text{ and } 260)$ nm. At high q , ω_p saturates at 0.9 eV.

Supplementary information for
Intrinsically Ultrastrong Light-Matter Interactions in Crystalline
Films of Carbon Nanotubes

Po-Hsun Ho, Damon B. Farmer, George S. Tulevski, Shu-Jen Han, Douglas M. Bishop, Lynne
M. Gignac, Jim Bucchignano, Phaedon Avouris, Abram L. Falk*
IBM T. J. Watson Research Center, Yorktown Heights, NY

* E-mail: alfalk@us.ibm.com

Table of contents

1. Properties of the nanotube suspension
2. Crystal structure of the nanotube films
3. Spectroscopy methods
4. Optical transitions of the crystalline nanotube films
5. Resistivity of the crystalline nanotube films
6. Supplementary References

1. Properties of the nanotube suspension

To verify that the nanotubes are indeed well dispersed in SDBS suspension, we have checked this suspension by drop-casting it on blank silicon chips, drying the chips, and imaging them with atomic force microscopy. No nanotubes whose height is greater than 2 nm are observed (Fig. S1), indicating that our sonication and centrifugation processes are effective at removing bundles from the suspension.

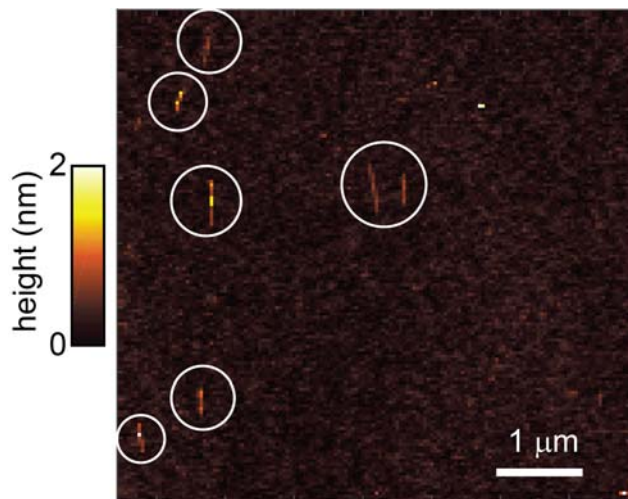


Figure S1 | Atomic force microscopy (AFM) image of nanotubes that are drop-casted and dried on a silicon chip. They are from an aqueous SDBS suspension that was used to fabricate our crystallized nanotube films.

2. Crystal structure of the nanotube films

With the modified vacuum filtration method, a one-inch crystalline nanotube film was deposited on a polycarbonate membrane (Fig. S2). As discussed in Ref. 23, this process could be readily extend to the wafer scale by using a larger fritted glass and membrane. Both the microscopic and macroscopic crystalline properties of this nanotube film were measured by selective area electron diffraction and grazing-incidence X-ray diffraction.

Fig. S3 (a) shows a cross-sectional TEM image of a crystalline nanotube film. We measured the selective area diffraction pattern in regions of this image (Fig. S3(a)). The corresponding diffraction patterns are shown in Fig. S3(b). Different crystal angles of hexagonal lattice were observed, indicating that this nanotube film is polycrystalline.

Grazing incidence X-ray diffraction (XRD) was used to further characterize the crystallinity of the aligned CNT arrays. The reason that the grazing incidence mode was chosen is that it is particularly effective at measuring thin films. Here, we focus on the low angle diffraction related to the >1 nm lattice constant from the lattice of nanotube (as opposed to the much higher angle diffraction coming from the carbon lattices of the comprising nanotubes).

The XRD was performed with a Siemens D5000 XRD spectrometer and a Cu-K α ($\lambda = 1.54$ Å) x-ray source. The incident angle was fixed at 2.2° , and the angle of the detector was swept. A strong discrete peak is observed at $2\theta = 5.8^\circ$, which corresponds with the lattice spacing of the aligned nanotube arrays. Based on the two-dimensional hexagonal lattice of nanotubes indicated by the selected area TEM diffraction (Fig. 1c, 1d, and Fig. S3b), this signal comes from the (10) plane of the lattice. The $d_{(10)}/a$ ratio is $\sqrt{3}/2$, where a is the lattice constant. Bragg's law, $2d \sin \theta = n\lambda$, therefore indicates that the lattice constant of the nanotube lattice is $a = 1.74$ nm. In light of the $D = 1.41$ nm average diameter of nanotubes, as specified by the nanotube manufacturer, the van der Waals gap between neighboring nanotubes, $a - D$, is 3.3 Å.

XRD measurements with the nanotube sample oriented in different directions relative to the incident light were also performed (Fig. S4A). The collected data are all indexed and shown in Fig. S4B. When the CNTs are parallel to the incident plane, the strongest (10) and (11) signals were obtained. However, the higher index signals were smaller than those corresponding to other alignment directions. These results confirm the preferred orientation direction of the polycrystalline CNT film.

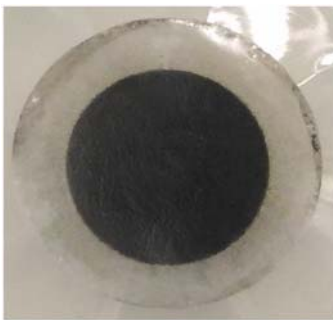


Figure S2 | A photograph of a 1-inch-in-diameter CNT film on a membrane.

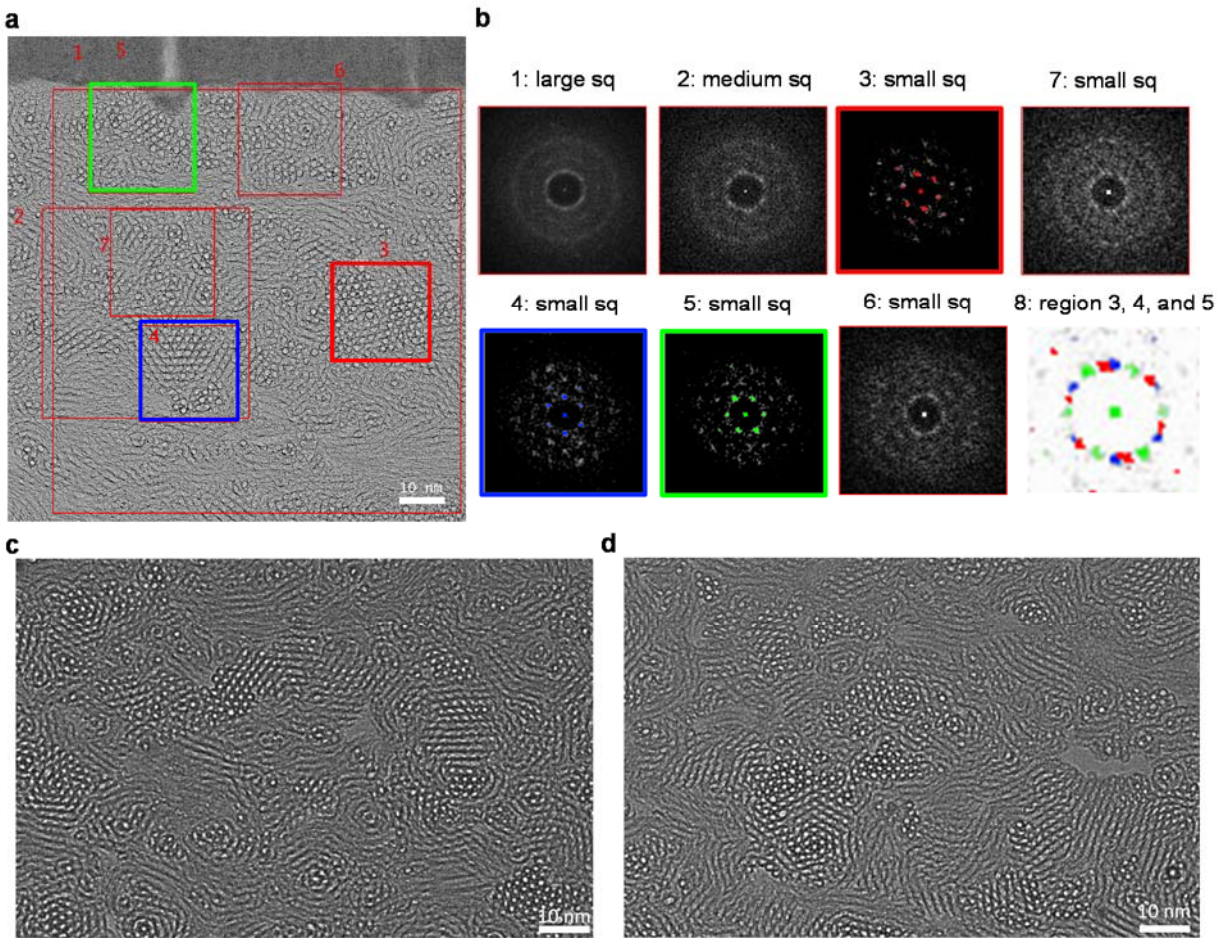


Figure S3 | Additional cross-sectional TEM images. **a.** A cross-sectional TEM image of the nanotube film shown in Figs. 1a-c. **b.** Selective area electron diffraction patterns (SAED), corresponding to the regions marked in A. In image #8, the locations of the diffraction spots regions 3, 4, and 5 are combined. **c.** and **d.** Cross-sectional TEM images of another nanotube film, also showing clear polycrystallinity.

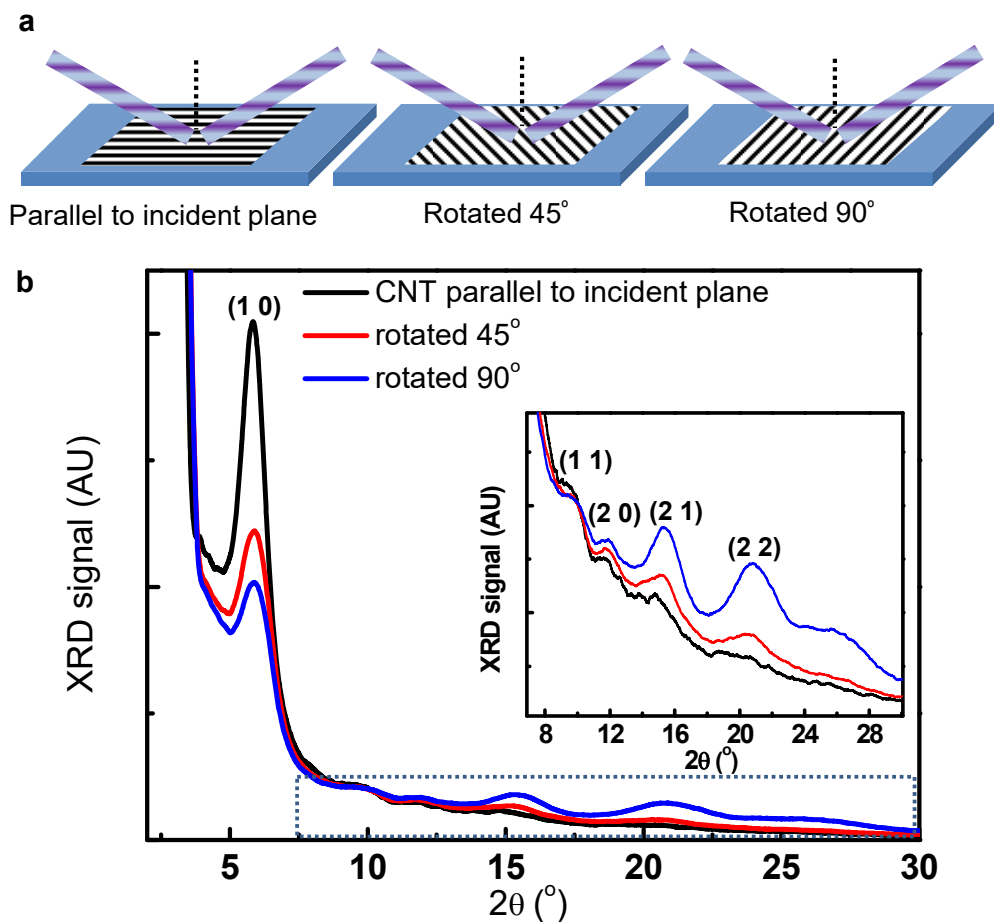


Figure S4 | Angle-dependent XRD measurements. **a.** Schematic images of XRD measurements with different orientations of the CNT film relative to the x-ray beam. **b.** XRD profile of the CNT film with different orientations. Inset: magnified image of the high angle region (dashed box in the main figure panel).

3. Spectroscopy methods

The extinction spectra were measured in a Bruker Nicolet 8700 μ -FTIR system. The diameter of the focused beam size is 100 μm , and each measurement was integrated for a 100-second period. Before each spectrum is taken, a background spectrum is taken, on an area of the chip in which the carbon nanotubes have been completely etched away. The spectrometer outputs absorbance relative to the background spectrum. The extinction is then calculated as

$$Extinction = 1 - 10^{-absorbance(\nu)}. \quad (S1)$$

Measurements of the high frequency plasmon resonances in thick films ($\nu_p > 7000 \text{ cm}^{-1}$, see Fig. 3d), which were out of the range of our FTIR system, were executed using a PerkinElmer Lambda 950 UV-VIS-NIR spectrometer. The films we prepared for use in this system were similar to the ones that we prepared for FTIR, except 1) larger patterns ($3 \text{ mm} \times 7 \text{ mm}$) were prepared, to accommodate the larger beam size of this spectrometer, and 2) sapphire substrates were used instead of silicon, to extend the range to higher energies.

Fig. S5a and b are the non-normalized (i.e. as-measured) extinction spectra corresponding to Figs. 2c and 2d. In both spectra, we observe that as the lithographically defined CNT length (L) becomes shorter, the extinction signal becomes less, even though a 1:1 nanotube:gap coverage ratio is maintained. The simplest explanation for this phenomenon is that, as L is reduced, there is an increasing wavevector mismatch between the nanotube resonators and free space. Another contributing factor may be damaged ends of the nanotubes arising from the reactive ion etching.

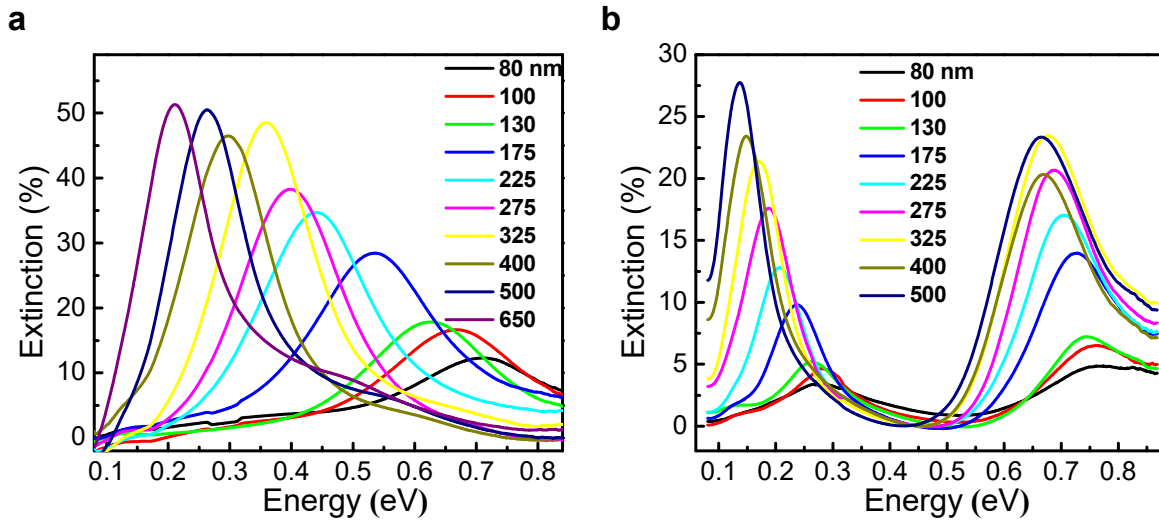


Figure S5 | Non-normalized extinction spectra of 49 nm-thick nanotube ribbons in **a.** a high doping-level state, and **b.** a low doping-level (annealed) state. The etched nanotube length (L) is given in the legends. In Figs. 2c-2d of the main text, we normalized the height of the extinction spectra and offset them from each other, for clarity of presentation. Here, we present the same data, except that we do not normalize the curves or offset them from one another.

4. Optical transitions of the crystalline nanotube films

We used an FTIR spectrometer to perform all the extinction spectroscopy in the main text. However, this instrument only measures energies up to 0.95 eV. To measure higher energy optical transitions in our crystalline nanotube films, we used a PerkinElmer Lambda 950 UV-VIS-NIR spectrometer. For these measurements, to avoid silicon absorption, we used sapphire substrates. The detection area of this system is 25 mm².

Figure S6 presents the UV-VIS spectra of a 20 nm-thick film with different doping levels. Three excitons can be clearly identified: the S_{11} and S_{22} excitons of semiconducting CNTs, and the M_{11} exciton of metallic CNTs. With increasing p -type free charge density, the S_{11} excitons are quenched first, due to depopulation of the highest-energy valence states. The S_{22} exciton is next to be quenched. At very high doping levels, the selection rules of the optical transitions are modified, allowing new inter-valance-band transitions.^{S1} Therefore, new optical transitions can be observed. In our CNT film, we observe an inter-valance band transition S_{41} , whose energy is 1.04 eV. This state has previously been observed in strongly doped CNT films.^{S1,S2} These inter-valance excitons persist at high p -type doping levels and can strongly couple to plasmon resonances. They are likely responsible for the saturating resonance energies at 0.9 eV that are observed in Fig. 3d of the main text.

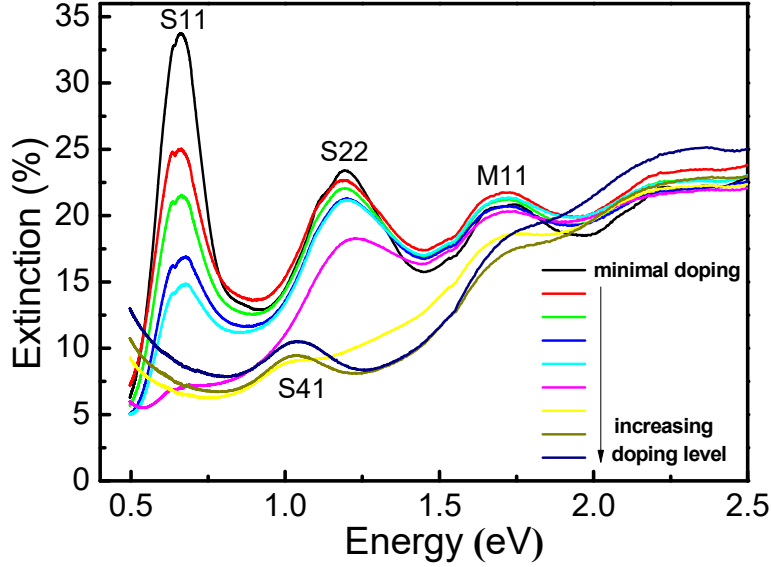


Figure S6 | UV-VIS extinction spectra of a 20-nm-thick CNT film, as a function of chemically induced charge-carrier density. Although S_{11} and S_{22} decrease in intensity with increasing doping level, a new peak, S_{41} , emerges at very high doping levels.^{S1,S2}

5. Resistivity of the crystalline nanotube films

An in-line four probe method was used to measure the resistivity of our crystallized CNT films. For a film of thickness $t = 100$ nm, in its minimal doping state (i.e. measured right after it has been annealed in vacuum), the as-measured four-probe resistance is $R_x = 171 \Omega$, where R_x corresponds to the resistance in the nanotube alignment axis. The four-probe resistance measured perpendicular to the alignment axis (R_y) is four times higher than R_x . After the nanotube films are exposed to HNO_3 vapor, when the nanotube films are in a highly chemically doped state, R_x is reduced by a factor of 30.

To calculate the sheet resistivity, we model the CNT film as an infinite 2D sheet, and calculate the resistivity of nanotube film as $\rho_x = \frac{\pi}{\ln(2)} R_x t$. Using this formula, we calculate on-axis sheet resistivities of $7.6 \times 10^{-3} \Omega\cdot\text{cm}$ (after vacuum annealing) and $2.6 \times 10^{-4} \Omega\cdot\text{cm}$ (after HNO_3 vapor treatment). We note that, due to the anisotropy of the film, the factor of $\frac{\pi}{\ln 2}$, which accounts for the spread of current in the sheet, overestimates the true current spread in our film.

The resistivities that we report should thus be understood as conservative estimates that modestly overestimate the true resistivities of our films.

6. Supplementary References

- S1. Kim, K. K. *et al.* Fermi Level Engineering of Single-Walled Carbon Nanotubes by AuCl₃ Doping. *J. Am. Chem. Soc.* **130**, 12757–12761 (2008).
- S2. Shin, D. W. *et al.* A role of HNO₃ on transparent conducting film with single-walled carbon nanotubes. *Nanotechnology* **20**, 475703 (2009).